Surface Plasmons Phase Imaging Microscopy using Deep Learning

Suejit Pechprasarn[a], Suvicha Sasivimolkul[b], Chayanisa Sukkasem[c], Phitsini Suvarnaphaet[d] and Nuntachai Thongpance
College of Biomedical Engineering, Rangsit University, Phaholyothin Road, Pathum Thani, Thailand

Keywords: Surface Plasmon Resonance, Phase Imaging, Phase Retrieval Algorithm, Surface Plasmon Microscopy, Deep Learning, Image Recognition.

Abstract: Surface Plasmon Resonance have been a gold standard for biosensing and chemical sensing over the past decades. The surface plasmons are a confined electromagnetic wave mode propagating on surface of noble metals. One of the key features of surface plasmons is that they are sensitive to its surrounding medium, therefore the surface plasmons are usually applied in sensing applications. It has been very well established that measuring the phase response of the surface plasmons is more sensitive and more robust compared to intensity or amplitude measurements. To measure the phase, of course, an interferometer is required. This will impose the complexity to the optical alignment. Moreover, the interferometric systems usually require a well-controlled experimental condition, such as, vibration isolation system. Recently, there are some interest of the research community to recover the surface plasmons phase through computational phase retrieval algorithms, such as, Ptychography. Although these computational algorithms can recover the phase profile, they do require many images or a lengthy computing time making them not suitable for real-time measurement. Here, we propose a novel approach to perform surface plasmon phase retrieval using image recognition though deep learning. We demonstrate the feasibility of using the deep learning to recover amplitude and phase responses of simulated back focal plane images.

1 INTRODUCTION

Surface Plasmons (SPs) are a confined electromagnetic wave phenomenon propagating on surface of noble metals, such as, gold (Au), Silver (Al) and Copper (Cu) (Somekh & Pechprasarn, 2016). Surface Plasmon Resonance (SPR) is a well-known resonant effect of the SPs occurring when there is a p-polarized light beam (TM polarization) with a matching momentum to the resonant frequency of the SPs illuminating on the noble metal surface. The SPR is very sensitive to its local refractive index change around the height of 200nm from the metal surface due to the evanescent wave penetration depth of the SPs (Shen, Learkthanakhachon, Pechprasarn, Zhang, & Somekh, 2018). The SPs have been widely utilized as a gold standard equipment for label-free biosensing (Liedberg, Nylander, & Lundström, 1995), chemical sensing (Liedberg, Nylander, & Lunström, 1983) and bioimaging (Pechprasarn & Somekh, 2014; Somekh, Pechprasarn, Chow, Meng, & Shen, 2016).

There are two standard approaches to excite the SPs, which are (1) Kretschmann configuration (Kretschmann & Raether, 1968) as shown in Figure 1a and (2) Otto configuration (Akowuah, Gorman, & Haxha, 2009) as shown in Figure 1b. Both optical configurations require high index prism coupling and p-polarized incident illumination with the wavelength in red to infrared regime. The main difference between the two configurations is the thickness of the metal and the position of the metal. On the reflectance of both configurations, there will be a dark band in the reflectance curve, so called 'SP dip' position and the wave vector position that the SP dip occurs is the surface plasmon's wave vector or k_{sp}.

[a] https://orcid.org/0000-0001-9105-8627
[b] https://orcid.org/0000-0002-1459-8133
[c] https://orcid.org/0000-0003-4057-7237
[d] https://orcid.org/0000-0001-8195-1841

Pechprasarn, S., Sasivimolkul, S., Sukkasem, C., Suvarnaphaet, P. and Thongpance, N.
Surface Plasmons Phase Imaging Microscopy using Deep Learning.
DOI: 10.5220/0008917100330039
In *Proceedings of the 8th International Conference on Photonics, Optics and Laser Technology (PHOTOPTICS 2020)*, pages 33-39
ISBN: 978-989-758-401-5; ISSN: 2184-4364

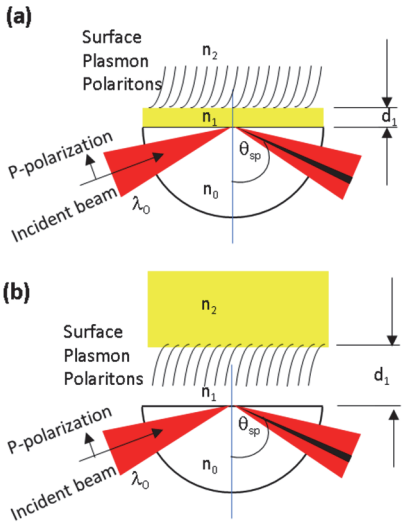

Figure 1: Shows conventional SPR optical setups (a) Kretschmann configuration and (b) Otto configuration.

The SP dip occurs due to loss mechanisms of SP coupling (Pechprasarn, Chow, & Somekh, 2018). This is a strong evidence for SP excitation. Figure 2a shows the simulated SP reflectance curves for different thicknesses of gold between 60nm to 60nm with the p-polarized incident wave of 633nm wavelength (HeNe) and the gold complex refractive index of 0.1834+3.4332i (Johnson & Christy, 1972) for Kretschmann configuration. Fig.2b shows corresponding phase responses. The phase responses of reflection coefficient for p-polarized wave were different for different thicknesses of the gold layer d_1. For the thicknesses lower than 47nm had 2π rad phase transition over the SP dip, whereas the thicknesses higher than 47nm had π rad phase transition. This can be explained by coupling strength of the SPs and the direct reflection from the gold surface, which is explained in detail in the cited reference here (Pechprasarn et al., 2018). The simulation results in Figure 2 were calculated using Fresnel equations and Transfer matrix approach (Suvarnaphaet & Pechprasarn, 2018).

For Kretschmann configuration, the uniform metal is usually very thin and attach to the glass prism layer. The metal thickness (d_1) for biosensing depends on the metal type and its application. For biosensing, gold is usually used as the SPR sensor chip, since gold is chemically stable and does not form an oxide layer with its environment (Suvarnaphaet & Pechprasarn, 2018). The gold thickness is usually employed at 46nm to 50nm, since it gives the darkest $|r_p|^2$.

On the other hand, for the Otto configuration there is a very thick metal layer positioned around one wavelength of light away from the glass prism. The Otto configuration to the best of author knowledge it is not usually applied in a biosensing. Most of its applications are in physics, like study of light-matter interaction (Pechprasarn et al., 2016).

Thanks to high numerical aperture (NA) objective lenses, which are becoming more affordable and widely commercially available, they have made the SPs excitation possible under a conventional microscope configuration as shown in Figure 3.

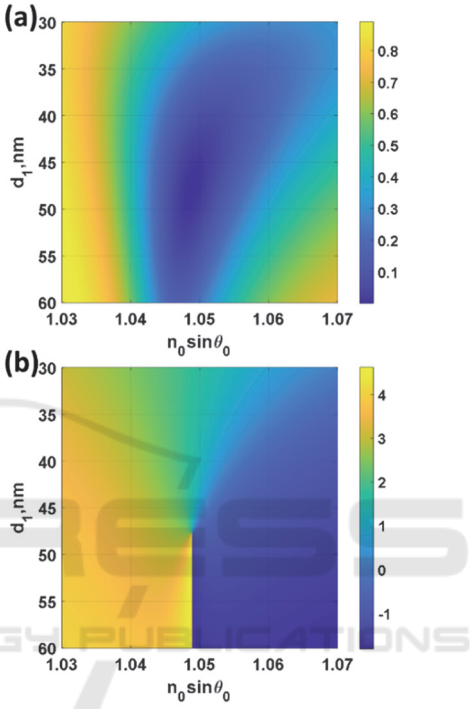

Figure 2: Shows (a) Reflectance $|r_p|^2$ and (b) phase of r_p in rad for 30nm to 60nm of uniform gold layer coated on BK7 glass with refractive index of 1.52. The incident wave was p-polarized wave at 633nm wavelength.

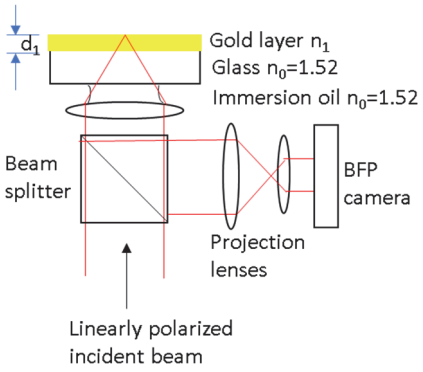

Figure 3: Shows gold sensor under an oil immersion objective lens and optical system to capture the back focal plane (BFP) image.

Figure 4a and Figure 4b show a simulated back focal plane (BFP) of the 1.49 NA objective lens microscope system in Figure 3a for a linearly polarized coherent source of 633nm wavelength. The pure p-polarization is along the x-axis of Figure 4 and the pure s-polarization is along the y-axis of Figure 4.

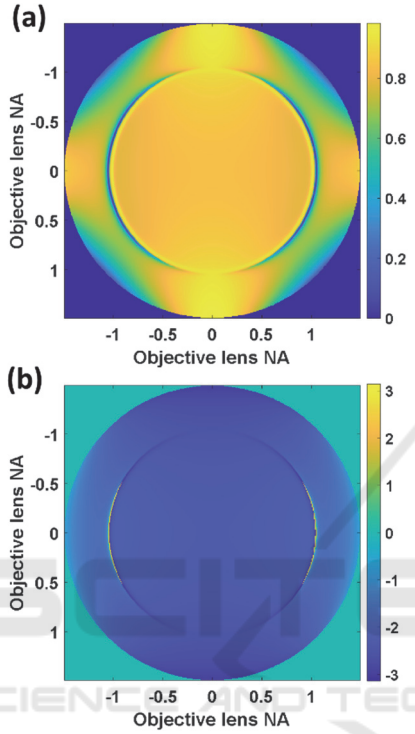

Figure 4: Shows (a) BFP intensity and (b) BFP phase in rad for the electric field component along x-direction. n0=1.52, n1=0.1834+3.4332i ,n2=1.00, d1=45nm λ0=633nm.

Although the SPR has been discovered and its theory have been thoroughly studied and very well established for a few decades, there are still new findings and breakthroughs reported over the recent years. One of the most exciting work in the field is single protein molecule imaging (Taylor & Zijlstra, 2017) and quantitative bioimaging (Tan, Pechprasarn, Zhang, Pitter, & Somekh, 2016). Most of the ultra-sensitive SPR systems rely on phase SPR phase measurement (Pechprasarn & Somekh, 2014). It has been very well established that in measuring SPR phase is more robust and more sensitive than measuring SPR amplitude response (Kabashin, Patskovsky, & Grigorenko, 2009). Of course, to measure the phase response, an optical interferometer is needed making the optical configuration more sophisticated (Pechprasarn, Zhang, Albutt, Zhang, & Somekh, 2014). There are several interferometric configurations reported to improve SPR phase measurement stability and repeatability, such as, common path SPR interferometry (Pechprasarn et al., 2014). Recently there is an interest in applying computational phase retrieval algorithms, such as, Ptychography (Somekh, Pechprasarn, Chen, Pimonsakonwong, & Albutt, 2017), Transport of intensity (Streibl, 1984) and Gerchberg and Saxton (Zalevsky, Mendlovic, & Dorsch, 1996) to retrieve the SPR phase with no requirement of an interferometer system.

Although the phase retrieval algorithms can be employed to recover the SPR phase, they still have their own disadvantages for each of the algorithms. For example, for the Ptychography and Gerchberg and Saxton they are iterative therefore they are not suitable for real time measurement. The transport of intensity method is not an iterative method, it recovers the phase by solving a Poison's equation to wave propagation to predict the phase of the propagating wave. The method requires finite element (FEM) calculation, computationally time consuming and require relatively large computing power compared to the other two methods.

Here, the mentioned issues will be addressed by replacing the time-consuming phase retrieval computations by a data driven technology deep learning. Here a 3 layered U-shaped artificial neural network (UNet) architecture was employed to learn how to do image segmentation and regression to predict the corresponding real part and imaginary part of the back focal plane as the network output.

2 PROPOSED METHOD

In this section, an overview of relevant computational methods and the deep learning are described in detail. There are 3 major components to train the UNet network (1) Input BFP intensity (2) the UNet network and (3) the labelled output BPF. Once the UNet has been trained and has reach its convergence. The network can then be deployed to validate itself, by predicting an output for a new BFP input. Validation to test the robustness of the trained network will be discussed in section 3.

2.1 Back Focal Plane Calculation

Here, 1,000 BFP images were computed with different d_1 thicknesses ranging from 25nm to 65nm serving as the training data for the UNet, which will be described in detail in the later section. The d_1 thicknesses are randomly distributed as shown in

Figure 5. The mean value and the standard deviation for the d_1 were 44.55nm and 11.33nm respectively.

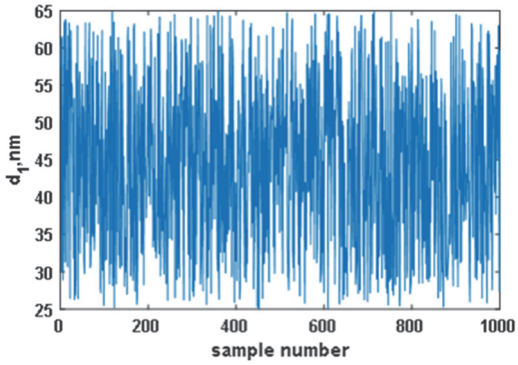

Figure 5: Shows d1 thicknesses for all the 1,000 cases.

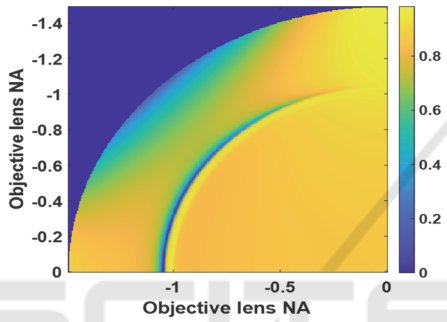

Figure 6: Shows one quadrant of the BFP intensity for the 500th sample with d_1 of 49.54nm.

BFPs for all the d_1 thicknesses were then computed using Fresnel equations and the transfer matrix approach (Suvarnaphaet & Pechprasarn, 2018). It is important to point out that only one quadrant of the BFP was computed to reduce the size of the training set since the other 3 quadrants contain the exact same information. Figure 6 shows a computed BFP intensity of the electric field pointing along x direction for the case number 500 (d_1 of 49.54nm). This is the input for the neural network.

For the output from the neural network, the labelled data was prepared as the real part and the imaginary part of the BFP as shown in Figure 7a and Figure 7b. The training dataset for the neural network consisting of 1,000 images with 1 input (BFP intensity with the size of 328 pixels x328 pixels) and 2 outputs (the real part of the BFP and the imaginary part with the total size of 328 pixels x328 pixels x 2 dimensions). It is important to point out that one can use only one output by taking the phase as the output, but here the two outputs was implemented to avoid the ambiguity of 2π rad phase wrapping. This will be discussed in detail in discussion section later.

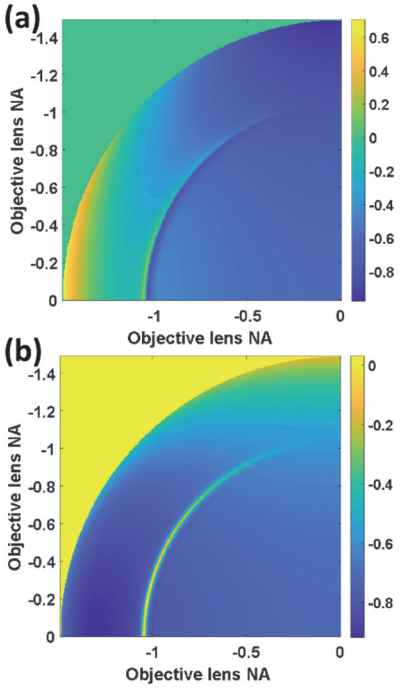

Figure 7: Shows (a) real part of the 500th sample BFP and (b) imaginary part of the 500th sample BFP.

2.2 U-Network Shape Neural Network

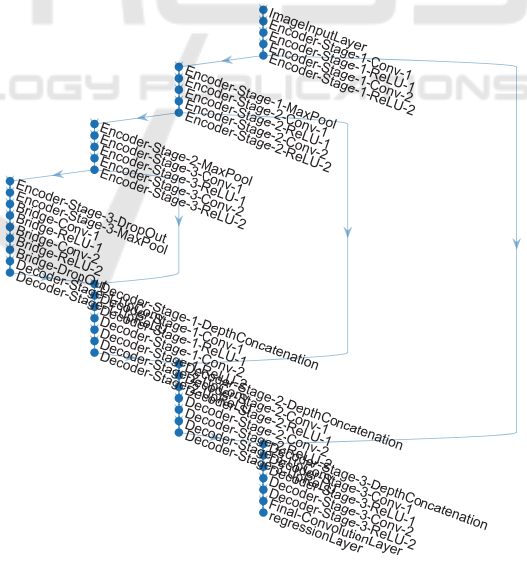

Figure 8: Shows U-shaped artificial neural network structure with 3 layers of encoders and 3 layers of decoders.

In this paper, U-shaped artificial neural network structure with 3 layers of encoder and 3 layers of decoder as shown in Figure 8 were employed. The UNet has been found to one of the best artificial neural networks (ANNs) for image segmentation and

image regression. Predicting the phase values is, of course, in the category of image regression. The detailed functions for each network layer are omitted they are all standard functions in deep learning. The UNet is then trained with the BFP dataset described in the section 2.1.

3 RESULTS AND DISCUSSION

3.1 Network Training

The UNet network was trained under MATLAB2019a environment with a single graphic processing unit (GPU) Nvidia GeForce GTX1060. It took about 8 hours for 100 Epoches (100,000 iterations in total). The UNet is trained so that the recovered outputs have reached the root mean square error less than 0.0001 or 0.01%.

Once the UNet is trained, in the next section the UNet will be tested with different thicknesses of d_1 to validate the corresponding output results.

3.2 Network Testing with Simulated Data

Here let us, see how well the network responses to the simulated input BFP. It is interesting to point out that the BFP phase responses do have different phase gradient and transition levels depending on the d_1 sensor thickness. Three thicknesses of 30nm,40nm and 50nm were chosen to be the test input to the trained UNet.

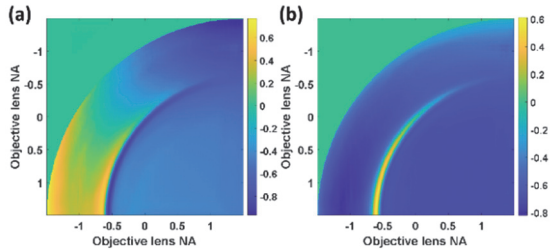

Figure 9: Shows (a) real part for d_1 of 30nm and (b) imaginary part for d_1 of 30nm.

The BFP images corresponding to the 3 thicknesses were then computed as discussed in section 2.1. The 3 BFPs were employed as an input to the trained UNet in turn. The output real part and imaginary part images corresponding to the 3 inputs are shown in Figure 9 to Figure 11 for d1 of 30nm, 40nm and 50nm respectively.

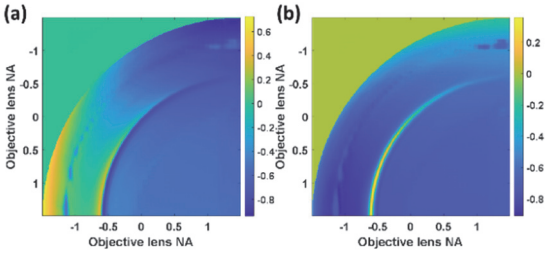

Figure 10: Shows (a) real part for d_1 of 40nm and (b) imaginary part for d_1 of 40nm.

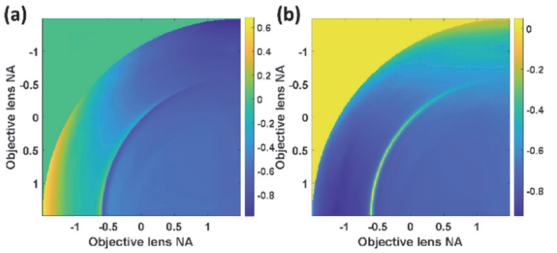

Figure 11: Shows (a) real part for d_1 of 50nm and (b) imaginary part for d_1 of 50nm.

The UNet can recover the real and imaginary parts for all the three inputs. However, for the 40nm case, there were some noise artefacts at around the NA of 1.02 for both s and p polarizations.

From the results in Figure 9 to Figure 11, the reflectance curve and the phase transition can be calculated as shown in Figure 12. Figure 12 shows the linescan reflectance $|r_p|^2$ for the 3 thicknesses.

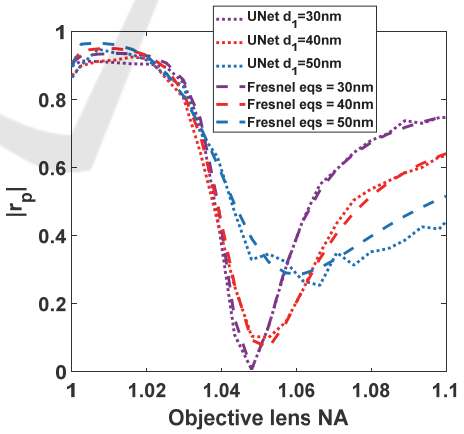

Figure 12: Shows linescan of recovered reflectance $|r_p|^2$ calculated from the results in Figure 9 to Figure 11 in comparison with the ideal BFPs calculated using Fresnel equations.

It can be observed that the recovered intensity images have the similar shape and intensity profiles compared to the Fresnel calculations. However, they did have some noise on the recovered SP dips

especially for 40nm case. The SP phase responses could also be recovered from the results in Figure 9 to Figure 11. The phase responses calculated from Fresnel equations for the three gold thicknesses are shown in Figure 13a in comparison with the phase profiles recovered from the UNet as shown in Figure 13a. Like the intensity responses, the recovered phase profiles using the UNet were like the phase profiles from Fresnel calculation with some random noise on the phase profile. These noises did not affect the shape and gradient of the phase transition of the SPR dip.

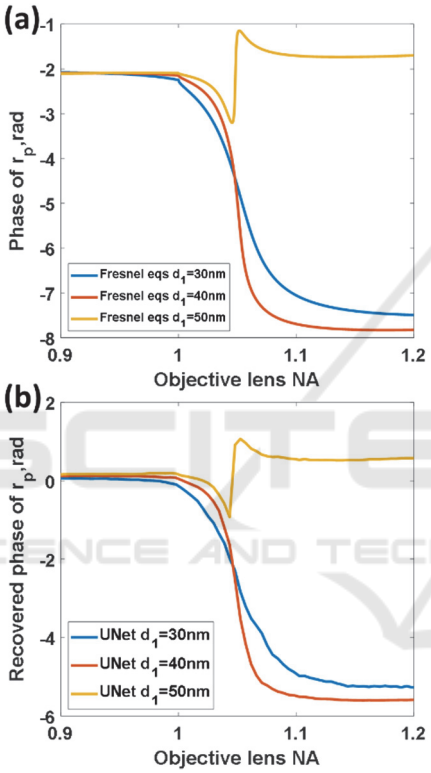

Figure 13: Shows (a) phase responses for the three thicknesses of gold calculated using Fresnel equations and (b) the recovered phase responses using the UNet.

The proposed image recognition using UNet might be another promising candidate to get around the issues of phase retrieval algorithms. There are still several issues that need to be further investigated, such as, how robust the network is at different input noise levels and its performance compared to the conventional interferometry and computational phase retrieval algorithms.

4 CONCLUSION

In this paper, we have proposed a novel approach to perform SPR phase measurement using U-shaped artificial neural network through deep learning. The UNet has been employed to replace the need for an interferometer or a computational phase retrieval algorithm. We have provided a theoretical analysis showing that the trained UNet can correctly recover different phase profiles. However, there are still some noise artefacts on the recovered intensity and phase profiles. There are still some room for further improvement, such as, training the network with a bigger dataset or including the image plane to the training set. We are currently investigating these possible improvements, which will be reported in another separate publication.

ACKNOWLEDGEMENTS

The authors would like to acknowledge the Research Institute of Rangsit University, Thailand for research funding and traveling grant.

REFERENCES

Akowuah, E. K., Gorman, T., & Haxha, S. (2009). Design and optimization of a novel surface plasmon resonance biosensor based on Otto configuration. *Optics express, 17*(26), 23511-23521.

Johnson, P. B., & Christy, R.-W. (1972). Optical constants of the noble metals. *Physical review B, 6*(12), 4370.

Kabashin, A. V., Patskovsky, S., & Grigorenko, A. N. (2009). Phase and amplitude sensitivities in surface plasmon resonance bio and chemical sensing. *Optics express, 17*(23), 21191-21204.

Kretschmann, E., & Raether, H. (1968). Radiative decay of non radiative surface plasmons excited by light. *Zeitschrift für Naturforschung A, 23*(12), 2135-2136.

Liedberg, B., Nylander, C., & Lundström, I. (1995). Biosensing with surface plasmon resonance—how it all started. *Biosensors and Bioelectronics, 10*(8), i-ix.

Liedberg, B., Nylander, C., & Lunström, I. (1983). Surface plasmon resonance for gas detection and biosensing. *Sensors and actuators, 4*, 299-304.

Pechprasarn, S., Chow, T. W., & Somekh, M. G. (2018). Application of confocal surface wave microscope to self-calibrated attenuation coefficient measurement by goos-hänchen phase shift modulation. *Scientific reports, 8*(1), 8547.

Pechprasarn, S., Learkthanakhachon, S., Zheng, G., Shen, H., Lei, D. Y., & Somekh, M. G. (2016). Grating-coupled otto configuration for hybridized surface phonon polariton excitation for local refractive index

sensitivity enhancement. *Optics express, 24*(17), 19517-19530.

Pechprasarn, S., & Somekh, M. G. (2014). Detection limits of confocal surface plasmon microscopy. *Biomedical optics express, 5*(6), 1744-1756.

Pechprasarn, S., Zhang, B., Albutt, D., Zhang, J., & Somekh, M. (2014). Ultrastable embedded surface plasmon confocal interferometry. *Light: Science & Applications, 3*(7), e187.

Shen, M., Learkthanakhachon, S., Pechprasarn, S., Zhang, Y., & Somekh, M. G. (2018). Adjustable microscopic measurement of nanogap waveguide and plasmonic structures. *Applied optics, 57*(13), 3453-3462.

Somekh, M. G., & Pechprasarn, S. (2016). Surface plasmon, surface wave, and enhanced evanescent wave microscopy. *Handbook of Photonics for Biomedical Engineering*, 1-41.

Somekh, M. G., Pechprasarn, S., Chen, W., Pimonsakonwong, P., & Albutt, N. (2017). *Back Focal Plane Confocal Ptychography.* Paper presented at the Applied Mechanics and Materials.

Somekh, M. G., Pechprasarn, S., Chow, W.-K., Meng, J., & Shen, H. (2016). *New avenues for confocal surface plasmon microscopy.* Paper presented at the Plasmonics in Biology and Medicine XIII.

Streibl, N. (1984). Phase imaging by the transport equation of intensity. *Optics communications, 49*(1), 6-10.

Suvarnaphaet, P., & Pechprasarn, S. (2018). Enhancement of long-range surface plasmon excitation, dynamic range and figure of merit using a dielectric resonant cavity. *Sensors, 18*(9), 2757.

Tan, H.-M., Pechprasarn, S., Zhang, J., Pitter, M. C., & Somekh, M. G. (2016). High resolution quantitative angle-scanning widefield surface plasmon microscopy. *Scientific reports, 6*, 20195.

Taylor, A. B., & Zijlstra, P. (2017). Single-molecule plasmon sensing: current status and future prospects. *ACS sensors, 2*(8), 1103-1122.

Zalevsky, Z., Mendlovic, D., & Dorsch, R. G. (1996). Gerchberg–Saxton algorithm applied in the fractional Fourier or the Fresnel domain. *Optics Letters, 21*(12), 842-844.